NDT&E International 139 (2023) 102936

Contents lists available at ScienceDirect

NDT and E International

journal homepage: www.elsevier.com/locate/ndteint

IMU-assisted robotic structured light sensing with featureless registration under uncertainties for pipeline inspection ☆

Mohand Alzuhiri[1], Zi Li [*,1], Adithya Rao, Jiaoyang Li, Preston Fairchild, Xiaobo Tan, Yiming Deng

Department of Electrical and Computer Engineering at Michigan State University, East Lansing, MI 48824, USA

ARTICLE INFO

Keywords:
Inertial measurement unit
Laser scanners
Measurement uncertainty
Registration
Structured light sensor
Wheel odometry
3D profiling

ABSTRACT

Laser profilometry and structured light sensors are being increasingly deployed for pipeline inspection as they provide the operator with a precise 3D map that can enable visual detection and direct insight into the integrity of the pipe. The focus of the presented paper is the design of an integrated robotic structured light sensing system used to improve the performance of 3D defect reconstruction for pipeline inspection while accommodating the uncertainty seen in a real-world environment. Point cloud registration of the consecutive 3D frames is a key factor in building this 3D map; therefore, a comprehensive featureless registration approach is proposed first, which is proven more efficient than conventional feature-based registration algorithms. Wheel odometry from the developed robotic platform and inertial measurements are integrated into the registration algorithm to enhance the 3D reconstruction performance for sensor stabilization. An intensity-based threshold searching method is further applied to retrieve the reconstructed defect size. Lastly, the uncertainties of the structured light sensing are investigated for the total reconstruction uncertainty and estimated measurement uncertainty to be quantified in order to illustrate the measurement precision. The efficacy of the proposed algorithms are supported by experimental results of pipeline inspection.

1. Introduction

Plastic pipes have become prevalent for the distribution of natural gas since the early 1970s and have been the primary material used as of 2017 [1]. Compared to the traditional steel pipe, which corrodes relatively easily, plastic pipes offer corrosion resistance and therefore superior durability for inside and outdoor use [2]. However, the rigidity and strength of plastic pipes are not comparable to those of steel pipes. This makes plastic pipes susceptible to damage from, for example, improper excavation or installation as well as from excessive stresses in the in-service environment of the pipe [3]. In addition, some of the disadvantageous material properties, such as higher thermal expansion coefficient when compared to metal and time and temperature dependence of material properties, make plastic pipes prone to elastoplastic fracture or plastic collapse, which can result in excessive deformation and cracks in the pipe [4]. These damages can lead to leaks and even explosions of gas pipes, which are high-level risks. Therefore, the detection and identification of deterioration in the material integrity of plastic pipe walls are of great significance.

Some nondestructive evaluation (NDE) based methods, such as ultrasonic testing [5,6], microwave testing [7,8], infrared thermography based methods [9,10], and camera-based visual inspection [11,12], have been developed and validated for the inspection of plastic pipes. However, each type of inspection method has its own limitations. The ultrasonic method typically needs a couplant during the inspection, which constrains the application scenarios. Microwave testing provides high resolution and accuracy, but the instruments and equipment of the sensing system are complex and expensive. The infrared thermography method may cause damage during the inspection since the material properties of plastic change with temperature. The visual inspection method, with the use of differing cameras, is an older but popular method. However, it requires a specific skill set of the operator and cannot quantify the depth of the damage to the plastic pipe. To remedy these limitations, a structured light (SL) sensor was developed by the authors for gas pipe inline inspection [13]. The original prototype of the SL sensor is suitable for performing the inspection only when the sensor is moving linearly with no change in orientation. However, in a

☆ This work was supported in part by the United States, Department of Transportation, Pipeline and Hazardous Materials Safety Administration (693JK31850007CAAP).

* Corresponding author.
E-mail addresses: lizi4@msu.edu (Z. Li), dengyimi@msu.edu (Y. Deng).

[1] The authors contribute equally to this paper.

https://doi.org/10.1016/j.ndteint.2023.102936
Received 29 December 2022; Received in revised form 10 June 2023; Accepted 10 August 2023
Available online 19 August 2023

real-world industrial application, such stringent requirements are often not feasible since the sensor is typically fitted on a moving platform (e.g., a robot), which will not be able to maintain such a strict pose while traversing the length of a pipeline. The proposed registration algorithm addresses this design gap and allows the SL sensing system to dynamically correct for changes in pose, resulting in a stabilized and accurate 3D reconstruction of wall profiles.

The designed SL sensor is attached to a scanning platform that moves along a pipeline during the internal 3D inspection. Every frame from the sensor produces data for a sparse reconstruction of the pipe surface with a density that is dependent on the number of projected rings. In an ideal scenario, the axis of the sensor is aligned with the main axis of the pipe and always points in the direction of platform movement, which is defined as the z-axis. Therefore, the reconstructed 3D frames can be stacked sequentially by only adding a displacement in the z-direction that is dependent on the scanner speed at the time of acquisition. Experimentally, this assumption is not practical because it is difficult to maintain position of the sensor exactly at the center of the pipe in the forward direction. Additionally, the speed of the platform is difficult to keep constant due to multiple uncertainties such as imperfections in mounting of the sensor to the robot, vibration from the movement of the robotic platform, and slippage of the robot wheels. Therefore, a holistic registration algorithm is required to estimate both the orientation of the sensor and its real-time position inside the pipe in order to realize accurate 3D reconstruction. For a pipe environment with defects, the localization of the sensor can be divided into two interconnected tasks:

- Global positioning: Localizing the identified damage with respect to the inspected pipe or pipeline network.
- Local positioning: Finding the geometrical transformation between consecutive frames from the sensor to reconstruct the surface, especially to characterize defects.

The main information sources for global positioning in an underground environment are the inertial measurements, wheel odometry, and anchor points inside the pipe (joints, connection, mains, etc.). Primary sources of information for local positioning include initial estimates of global positioning, refinements of 3D and 2D surface features, and known environmental constraints. Simultaneous localization and mapping (SLAM) algorithms, a popular global positioning method, allow the incremental creation of maps using data from sensors while estimating real-time positions [14,15]. While various methods have been applied to reduce mapping errors in SLAM, camera-based mapping with inertial navigation systems (INS) often have issues with the accuracy and drift of these systems [16]. For accurate global positioning in pipeline detection, the cylindrical nature of pipes are utilized as the basis for SL sensor-based localization [17]. Additionally, encoder data from the robot can provide accurate estimations on how far inside the pipeline the robot is [18].

After the global positioning is refined, the performance of the 3D reconstruction is related to the local positioning of the sensor as well. In this work, information from wheel odometry and IMU are incorporated to estimate the speed and orientation of the sensor in real time, which are able to realize a more reliable local positioning. The data is then fed into a registration algorithm to provide an initial estimate of the sensor orientation and position inside the pipe. Following this, a RANSAC-assisted [19] cylindrical fitting-based registration approach is utilized to provide high efficacy 3D point cloud registration to stabilize the sensor. This approach is preferred over using only features-based localization because it provides relatively accurate location and orientation estimation even when visual features (defects) are absent, which is common in plastic gas pipelines. With the stabilized sensor, the data registration is capable of calculating any shift and rotation of the sensor.

The remaining sections of the paper are organized as follows: Section 2 presents background information on the designed SL sensor, and then provides a detailed description of the point cloud registration. Section 3 describes the proposed cylindrical fitting-based 3D registration method with the introduction of a robotic integration system with external wheel odometry and IMU. An in-depth analysis of the uncertainty in this system is also provided in this section. Then a quantitative and qualitative evaluation of the proposed registration method is evaluated with experimental data in Section 4, while the initial uncertainty analysis is conducted to prove the high reliability of the system. A conclusion is presented in Section 5.

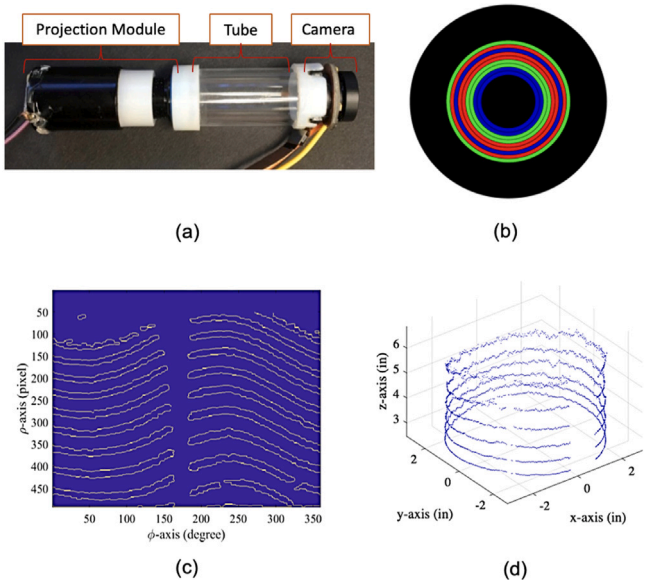

Fig. 1. (a) Fabricated endoscopic SL sensor; (b) Multi-color multi-ring slide pattern created from the color-coded sequence; (c) Extracted edges of the dark slits; (d) 3D reconstruction of the acquired example image. (For interpretation of the references to colour in this figure legend, the reader is referred to the web version of this article.)

2. Background

2.1. Structured light sensor

A structured light (SL) sensor consists of a projection module that projects a highly textured pattern and a camera that captures the deformations in the projected pattern [20]. A detailed description of the SL sensor design and fabrication is addressed in our previous work [13]. It consists of a camera module, a projector module, and a connected transparent glass tube for enabling the projection of the colored rings to the pipe walls, as shown in Fig. 1. The projector module consists of a high-intensity light-emitting diode (LED), a collimation lens, a transparency slide, and a projection lens. The Complementary metal–oxide–semiconductor (CMOS) camera is used to monitor the pipe surface and capture deformations in the projected rings. The 3D imaging reconstruction of the scanned object surface, as discussed in [20], is the process of detecting, localizing, and matching the projected edges. In this process, the acquired image is converted to the polar domain to perform edge detection based on the predefined color coding of the slide pattern. The dark slits are separated while the edges are extracted for localization, as shown in Fig. 1(c) . With essential cleaning and filtering, the extracted edges of each acquired image are reconstructed into a cylindrical shape in the 3D domain, which provides a basis for point cloud registration between data frames, presented in Fig. 1(d).

2.2. Point cloud registration

While the sensor is moving inside the pipe, each image frame produces a sparse reconstruction of the pipe surface with a density that

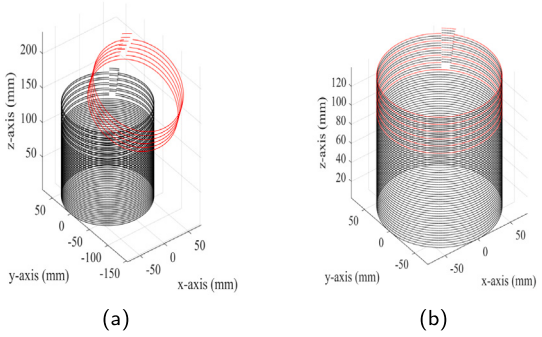

Fig. 2. Illustration of the point cloud registration problem. (a) Point clouds associated with fixed (black) and moving (red) frames; (b) Merged point clouds following proper registration of the moving frame. (For interpretation of the references to colour in this figure legend, the reader is referred to the web version of this article.)

is dependent on the number of projected rings. The 3D registration in this paper is categorized as a rigid registration problem, where two rigid frames need to be merged as depicted in Fig. 2(a). The black points represent the main fixed point cloud and the red points represent the new points on the moving frame that need to be merged with the main point cloud. Registration of these frames is shown in Fig. 2(b) where the moving frame is rotated and shifted to merge within the fixed frame.

The primary goal of the registration algorithm is to estimate the rigid geometrical transformation that registers the data from the moving frame to the data in the fixed frame. The geometrical transformation consists of rotation and translation in the 3D space. Therefore, the data in the moving frame ($\mathbf{D_M}$) is described by

$$\mathbf{D_F} = [\mathbf{R}|\mathbf{T}]\mathbf{D_M}, \tag{1}$$

where $\mathbf{R}$ and $\mathbf{T}$ are the rotation matrix and the translation vector respectively, and $\mathbf{D_F}$ is the data representation of the moving frame in the fixed frame coordinates. $\mathbf{R}$ is a 3×3 orthogonal matrix and $\mathbf{T}$ is 3×1 column vector.

3. Comprehensive 3D registration method

In this section, the proposed featureless-based 3D registration is introduced. The rotation matrix in Eq. (1) can be decomposed into its three main components:

$$\mathbf{R} = \mathbf{R_x}\mathbf{R_y}\mathbf{R_z}, \tag{2}$$

where

$$\mathbf{R_x} = \begin{pmatrix} 1 & 0 & 0 \\ 0 & \cos(\phi_x) & -\sin(\phi_x) \\ 0 & \sin(\phi_x) & \cos(\phi_x) \end{pmatrix},$$

$$\mathbf{R_y} = \begin{pmatrix} \cos(\phi_y) & 0 & \sin(\phi_y) \\ 0 & 1 & 0 \\ -\sin(\phi_y) & 0 & \cos(\phi_y) \end{pmatrix},$$

$$\mathbf{R_z} = \begin{pmatrix} \cos(\phi_z) & -\sin(\phi_z) & 0 \\ \sin(\phi_z) & \cos(\phi_z) & 0 \\ 0 & 0 & 1 \end{pmatrix}.$$

$\mathbf{R_x}$, $\mathbf{R_y}$, $\mathbf{R_z}$ are 3×3 rotation matrices that describe the rotation of the moving frame around x, y, and z axis, respectively, and ϕ_x, ϕ_y, ϕ_z are the corresponding rotation angles. The translation vector also has three main components

$$\mathbf{T} = [T_x, T_y, T_z], \tag{3}$$

where T_x, T_y, T_z represent the displacement in the x, y, z directions, respectively. Since an infinite cylindrical surface is assumed, and with the assistance of inertial measurements, there is no need to estimate the rotation around the z-axis or the shift along the z direction. Therefore, in this paper, the rigid transformation components are estimated through a cylindrical fitting, which is used to estimate $\mathbf{R}_x, \mathbf{R}_y$, and T_x, T_y.

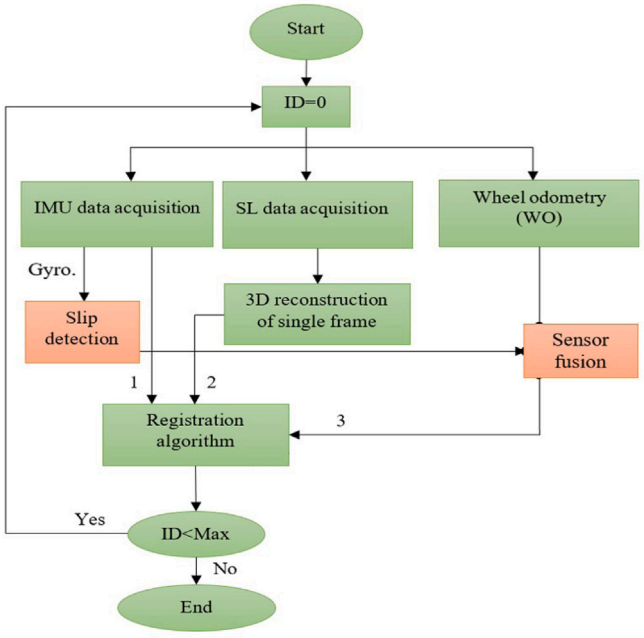

Fig. 3. Proposed registration approach for sensor stabilization with data acquisition procedure.

To find the geometric transformation, the registration algorithm depends on both inertial measurements and the matching of the common features in the fixed and moving frames. The main framework of the proposed registration algorithm for sensor stabilization can be summarized in Fig. 3 with two main interconnected tasks: local positioning and global positioning. In this scheme, the use of a synchronized acquisition framework is realized with real-time 3D point cloud data which is assisted by IMU and wheel odometry data. Global positioning provides a rough estimate of the pose (position and orientation) of the sensors inside the pipe by using wheel odometry and inertial measurements. This data is fed to a registration algorithm to provide an initial guess about the pose of the sensors inside the pipe. The 3D information is then used to provide a more precise tuning. If defect features are found, the global position is updated and the data is registered; otherwise, the initial global position is used in addition to the constraints from the cylindrical 3D environment.

3.1. Cylindrical fitting

The 3D points from a sensor inside a pipe are assumed to belong to an arbitrary infinite cylinder ($\mathbf{D_{arb}}$). This is a simplified assumption that ignores the existence of surface defects, which is a problem that will be accounted for separately. Therefore, in this method the prior pipe shape geometry is a basis to realize a non-feature-dependent 3D registration. A cylinder parallel to the z-axis that is centered around zero in the x–y plane is described as $\mathbf{D}$. An infinite cylinder ($\mathbf{D_{arb}}$) with an arbitrary orientation can be described as the cylinder ($\mathbf{D}$) that is rotated by a rotation matrix $\mathbf{R}$ and shifted by a translation vector ($\mathbf{T_{Cyl}}$)

$$\mathbf{D}_{\text{arb}} = \mathbf{R}\mathbf{D} + \mathbf{T}_{\mathbf{Cyl}}, \tag{4}$$

where

$$\mathbf{R} = \mathbf{R_x}\mathbf{R_y}, \tag{5}$$

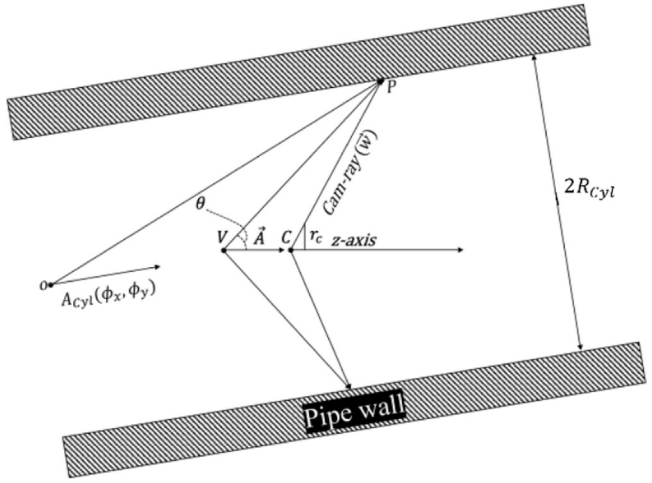

Fig. 4. Triangulation of structured light sensor inside a pipe environment.

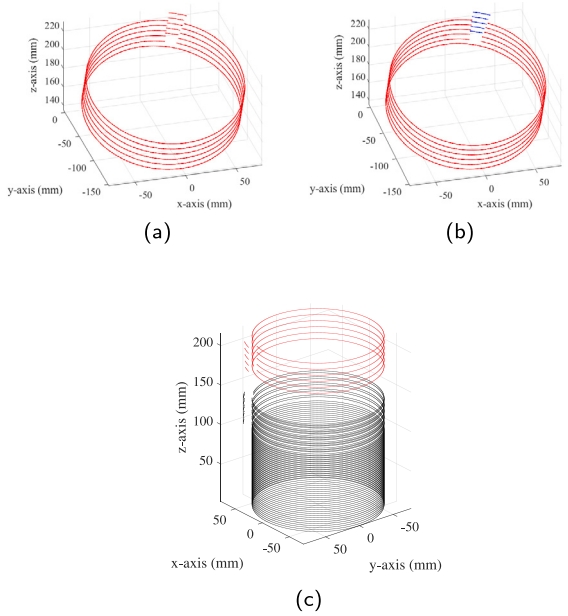

Fig. 5. Alignment correction with cylindrical fitting, (a) Input moving frame; (b) Moving frame with isolated defect by RANSAC in blue; (c) Point clouds after alignment correction, Red: Moving frame, Black: Fixed frame. (For interpretation of the references to colour in this figure legend, the reader is referred to the web version of this article.)

$$\mathbf{T}_{Cyl} = [\mathbf{T_x}, \mathbf{T_y}]. \tag{6}$$

From the above equations, the transformation is not a function of the shift and rotation around the z-axis; therefore, the number of parameters in the rigid transformation is reduced to ϕ_x, ϕ_y, T_x, and T_y only. A direct solution to fitting a cylinder to the point cloud can be found by minimizing the variance of the estimated radius of the pipe ($\hat{\mathbf{r}}_{\mathbf{Cyl}}$) from the estimated 3D points ($\hat{\mathbf{D}}$). Therefore, the minimization problem is described by

$$(\phi_x, \phi_y, T_x, T_y) = argmin(Var(\hat{\mathbf{r}}_{\mathbf{Cyl}})), \tag{7}$$

and any point on the surface of estimated $\hat{\mathbf{D}}$ satisfies

$$\hat{r}_{Cyl_i} = \sqrt{\hat{D}_{x_i}^2 + \hat{D}_{y_i}^2}, \tag{8}$$

$$\hat{\mathbf{r}}_{\mathbf{Cyl}} = [r_{Cyl_1}, r_{Cyl_2}, r_{Cyl_3}, \dots ..., r_{Cyl_n}]. \tag{9}$$

In this paper, sensor characteristics are integrated into the 3D registration problem to improve the robustness of the fitting performance. The environment inside the pipe is described in Fig. 4, where a calibrated structured light sensor is enclosed by a cylinder with a radius $\mathbf{R_{Cyl}}$, while each projected ring by the SL projector is assumed to be an acute cone with the main axis direction described by a unit vector $\vec{\mathbf{A}}_{\mathbf{Cyl}}$. In this environment, the camera is located at the origin ($C = (0, 0, 0)$) of the coordinate system and the camera is pointing along the z-axis. The projected ring is imaged by the camera to create a set of image points ($\mathbf{D_C}$) that can be represented by the camera ray ($\vec{w}$). The camera rays intersect with both the projected cone from the projector module and the surface of the bounding cylinder. Therefore, the intersection points belong to both the cylinder and the cone surfaces. With known cylinder parameters (), the intersection between the camera ray and the cylindrical surface can be easily calculated with the substitution of the ray equation in the cylinder equation. Therefore, the cylinder orientation can be calculated by minimizing the difference between $\mathbf{D_C}$ and $\mathbf{D_{arb}}$, which can be described by

$$(\phi_x, \phi_y, T_x, T_y) = argmin(\|(\mathbf{D_{arb}} - \mathbf{D_C})\|_2^2). \tag{10}$$

One source of error that affects the accuracy of the cylindrical fitting is the existence of artifacts on the pipe wall since the fitting process assumes an ideal cylindrical surface. The defect causes the fitting algorithm to be biased and results in an inaccurate estimation of the cylinder parameters; therefore, the problem is more prominent when having deep defects in the pipe wall [13]. To reduce the effect of wall defects, the defects are assumed to be outliers that need to be identified and removed from the fitting problem. In this case, random sample consensus (RANSAC) was applied. RANSAC is an iterative method that estimates the model parameters in the existence of outliers by separating them from inliers with repeated random subsampling [19]. Therefore, all the defects are separated as they do not fit the cylindrical model that is assumed during the optimization process. The fitting process of simulation is presented in Fig. 5, where the input frame to the fitting process with a cylinder diameter of 6 inches (76.2 mm) and a wall defect of a depth of 10.16 mm. Fig. 5(b) shows the isolated defect region with RANSAC, while the actual rotation angle is around the z axis. The algorithm can successfully isolate the defect region from the rest of the cylindrical surface. After isolating the defect data, the cylindrical surface data is fitted and the rigid transformation parameters are calculated.

The output of this stage is described in Fig. 5(c) where it shows two point clouds that are aligned along the z-axis and are centered around the origin.

3.2. Inertial measurements

The IMU is unable to provide an absolute 3D position of the sensor by itself, but it can provide linear acceleration, angular velocity, and orientation information. Due to the integrative nature of the position calculation, the error in the position estimation accumulates over time, especially in the case of small-size low-end IMU sensors. Therefore, using accelerometer data for distance estimation is not a reliable solution for this use case. The IMU also combines readings from the magnetometer and gyroscope to estimate the orientation of the IMU in 3D space, which is used to estimate the rotation angle of the sensor inside the pipe.

3.2.1. Gyroscope-camera calibration

The gyroscope camera calibration is needed to estimate the rigid transformation between the camera and gyroscope readings. This enables a direct translation of the rotation in the gyroscope reading to a rotation in the camera/sensor frame.

In this paper, a practical calibration approach is developed to simplify the optimization problem for handling a smaller number of unknowns than conventional methods:

1. Ignore the effect of the camera rolling shutter by performing the calibration with slow sensor movement and using the move and hold procedure. This is a realistic assumption since the sensor experiences rolling shutter behavior only outside the pipe when it cannot utilize the synchronized LED illumination.
2. Since synchronized camera and IMU acquisition and the move and hold procedure are utilized, the delay between the acquisition of the camera frame and the IMU reading is negligible.
3. The gyroscope is also internally calibrated, therefore there is not a need to calculate the gyroscope bias.

With these constraints, the calibration issue can be dealt with as an eye-hand calibration problem. Similar to hand-eye calibration, the calibration is aided by a calibration board to facilitate estimating the position of the camera and its orientation in the 3D world. Any rotation of the camera leads to a rotation in the original camera data $\mathbf{D}$ as follows:

$$\mathbf{D_c} = \mathbf{R_c}\mathbf{D}. \tag{11}$$

where $\mathbf{R_c}$ is a rotation matrix describing the rotational change in the obtained rotated camera data $\mathbf{D_c}$. Similarly, for the IMU data acquisition,

$$\mathbf{D_c} = \mathbf{R_{cal}}\mathbf{D_{cm}}, \tag{12}$$

$$\mathbf{D_{cm}} = \mathbf{R_m}\mathbf{R_{cal}^T}\mathbf{D}. \tag{13}$$

where $\mathbf{R_{cal}}$ is the calibration matrix which is the transformation matrix from the obtained camera data $\mathbf{D_c}$ to IMU frame $\mathbf{D_{cm}}$, and $\mathbf{R_m}$ is a rotation matrix for the change in rotation in the IMU frame, which is obtained from the IMU readings.

Therefore, combining Eqs. (12) and (13), the relationship between $\mathbf{R_c}$ and $\mathbf{R_m}$ can be inferred as follow:

$$\mathbf{D_c} = \mathbf{R_{cal}^T}\mathbf{R}_m\mathbf{R_{cal}}\mathbf{D} = \mathbf{R_c}\mathbf{D}, \tag{14}$$

$$\mathbf{R_c} = \mathbf{R_{cal}^T}\mathbf{R_m}\mathbf{R_{cal}}. \tag{15}$$

During the calibration process, camera and gyroscope data is collected with a calibration board in the field of view of the camera to provide a camera pose. If two consecutive frames from the system are examined, there will be two states:

$$\text{State 1 (frame1)}: O_{c1},\ O_{m1},\ D_{c1}, \tag{16}$$

$$\text{State 2 (frame2)}:\ O_{c2},\ O_{m2},\ D_{c2}, \tag{17}$$

where O_c is the orientation of the camera, O_m is the orientation measured by IMU and D_i is data generated by line-plane intersection. According to Eq. (15):

$$\mathbf{R_c}\mathbf{R_{cal}^T} = \mathbf{R_{cal}^T}\mathbf{R_m}. \tag{18}$$

Since the camera has already been calibrated, $\mathbf{R_c}$ and $\mathbf{R_m}$ are known and only $\mathbf{R_{cal}}$ needs to be solved for. The equation can be arranged to have the form $\mathbf{Ax} = \mathbf{0}$, and the value of $\mathbf{x}$ can be found by finding the null space of the set of homogeneous equations. However, upon further examination of the problem, it was noticed that adding noise leads to a failure of the solver to find any solution other than the trivial solution. The problem is ill-posed [21] and the matrix $\mathbf{A}$ has a large condition number (2.7×10^{16} from simulated data) which means that a small change in the input can lead to a large change in the output. To handle this problem, the approach proposed by Tsai and Lenz [22] is used to solve $\mathbf{Ax} = \mathbf{xB}$ problems which provide a more stable and regularized solution.

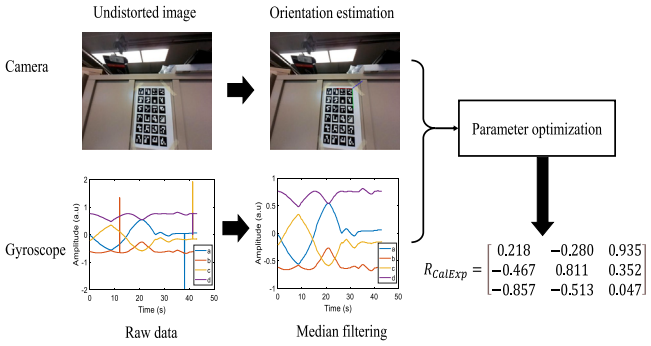

Fig. 6. Gyroscope calibration process with the help of vision-based orientation estimation.

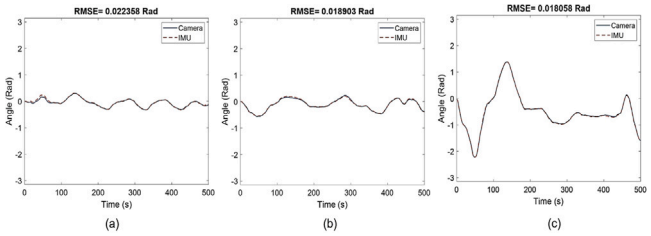

Fig. 7. Comparison between the ground truth from the camera and the estimated orientation from the IMU, (a) Rotation around the x-axis; (b) Rotation around the y-axis; (c) Rotation around the z-axis.

For the experimental setup, 500 camera-IMU frame pairs were collected to serve as input to the calibration algorithm. For the camera-based localization, Aruco patterns were used because they can be decoded even with partial occlusions to the calibration boards. The camera is first calibrated then each camera frame is flattened to remove the effect of lens distortion. With known camera intrinsic parameters and calibration board pattern, the board orientation can be calculated by using the Perspective-n-Point approach. The change in the camera orientation equals the inverse of the change in the orientation of the board. A schematic explaining the calibration process is shown in Fig. 6. The gyroscope data was collected in quaternion form as four-channel time series and a median filter was then applied to reduce the effect of salt and pepper noise. Since the change in rotation is of interest instead of the actual orientation, the difference in the rotation between every two consecutive frames is calculated as follows:

$$\mathbf{R_{x_i}} = \mathbf{R_i} + \mathbf{1}\mathbf{R_i^T}, \tag{19}$$

where $\mathbf{R_i}$ refers to the rotation matrix of the ith frame and $\mathbf{R_{x_i}}$ is the difference in the rotation between every two consecutive frames. A more stable approach was to measure the difference in rotation with respect to the first frame $\mathbf{R_1}$ and it is given by

$$\mathbf{R_{x_i}} = \mathbf{R_{i+1}}\mathbf{R_1^T}. \tag{20}$$

This approach depends on the absolute pose provided by the sensor instead of depending on the frame-to-frame difference. The absolute pose method shows better performance with a RMSE reduction of 10%. The improvement can be related to the effect of the filtering algorithm in the sensor which corrects the error over time adaptively. The results of applying the calibration matrix to the IMU data are shown in Fig. 7. These results shown satisfactory calibration for all the axis with RMSE values of the error ranging from 0.019 to 0.022 radians. It is worth noting that tracking the rotation around the x-axis and y-axis is not a priority since the main interest is in checking if the sensor has rotated around the main pipe axis (z-axis).

3.2.2. Usage of the IMU data

Once the calibration parameters are known, the IMU data can be used to monitor the sensor orientation, which is further integrated for sensor orientation correction, with the following algorithm: In the beginning, a reference frame (frame 1) is marked and its orientation can be described by:

$$\mathbf{R}_{\mathbf{c}_1} = \mathbf{R}_{\mathbf{cal}}^{\mathbf{T}} \mathbf{R}_{\mathbf{m}_1} \mathbf{R}_{\mathbf{cal}}, \tag{21}$$

where $\mathbf{R}_{\mathbf{m}}$ is a rotation matrix for the change in rotation in the IMU frame, and $\mathbf{R}_{\mathbf{c}}$ is a rotation matrix for the change in rotation in the camera frame. $\mathbf{R}_{\mathbf{m}_1}$ is the initial IMU frame, which gives the initial rotation in the camera frame $\mathbf{R}_{\mathbf{c}_1}$. Any consecutive frame (frame i) orientation is described by:

$$\mathbf{R}_{\mathbf{c}_i} = \mathbf{R}_{\mathbf{cal}}^{\mathbf{T}} \mathbf{R}_{\mathbf{m}_i} \mathbf{R}_{\mathbf{cal}}, \tag{22}$$

Relative rotation between the initial frame and the current frame i is given by

$$\mathbf{R}_{\mathbf{cm}_i} = \mathbf{R}_{\mathbf{c}_1}^{\mathbf{T}} \mathbf{R}_{\mathbf{c}_i}, \tag{23}$$

This can then be applied to correct the original data $\mathbf{D}_{\mathbf{c}_i}$ provided by the IMU to obtain the corrected data frame $\mathbf{D}_{\mathbf{cm}_i}$ to compensate for the actual sensor rotation as follow:

$$\mathbf{D}_{\mathbf{c}_i} = \mathbf{R}_{\mathbf{cm}_i}^{\mathbf{T}} \mathbf{D}_{\mathbf{cm}_i}. \tag{24}$$

3.3. Wheel odometry

Another set of sensors utilized for localization is the wheel odometers as an additional input to estimate the speed and position of the platform. The sensor position is estimated according to the number of wheel rotations at the ith frame $w_r(i)$, and its diameter d. Therefore, the estimated instantaneous position at frame i relative to the initial location is given by

$$T_{od}(i) = w_r(i)\pi d. \tag{25}$$

The estimated distance DIS_i between the ith and the previous frame is given as:

$$DIS_i = T_{od}(i) - T_{od}(i-1). \tag{26}$$

In the experimental setup, a robotic platform is utilized to maneuver the structured light inside the pipeline. For linear movement inside the pipeline, the robot uses three pairs of wheels, with each set of wheels connected to a dedicated encoder. The robot with highlighted encoders is shown in Fig. 8(a); while the integrated SL sensor is attached at the side opposite to the Raspberry Pi, shown in Fig. 8(b). 3D printed material and the necessary electronics were integrated with the robot for operation. The robot is powered by two attached sets of 14.4v LiPo batteries. These batteries provide the necessary power to the motors, structured light projectors, and other electronics, enabling them to operate untethered. The control board used for operation is a Raspberry Pi 4B, with GPIO pins used to control output to motors, read IMU and encoder data, and switch LEDs of the structured light sensor on and off. The Raspberry Pi allows for remote connection via Wi-Fi for remote controllability of the robot. The robot is driven by 5 sets of N20 motors with encoders. The middle three sets of motors are used for forwarding and backward directional movement inside the pipeline. The motors are connected to 7 PPR magnetic encoders and are geared down at a ratio of 603:1. This provides for a very high resolution on the rotation of the output shaft of the motor. The motors are attached to Omni wheels that reduce the amount of torque required to rotate the robot inside the pipeline. The end two motors are attached to free-rolling hemispherical wheels that rotate along the edge of the pipe to provide the necessary torque to achieve rotation inside the pipe. The use of three encoders improves the robustness of the data because the probability of three wheels slippage is lower than the probability of the slippage of a single wheel. In this paper, the median distance between frames of the three encoders are used as the reference distance estimate for the entire robot. Utilizing the median can reduce effects from wheel slippage producing an artificial distance increase or from motor stalling decreasing the distance. In this work, the robot-integrated sensing system was deployed in the 6-inch PVC pipe, which is shown in Fig. 8(c), whose performance will be analyzed in subsequent sections.

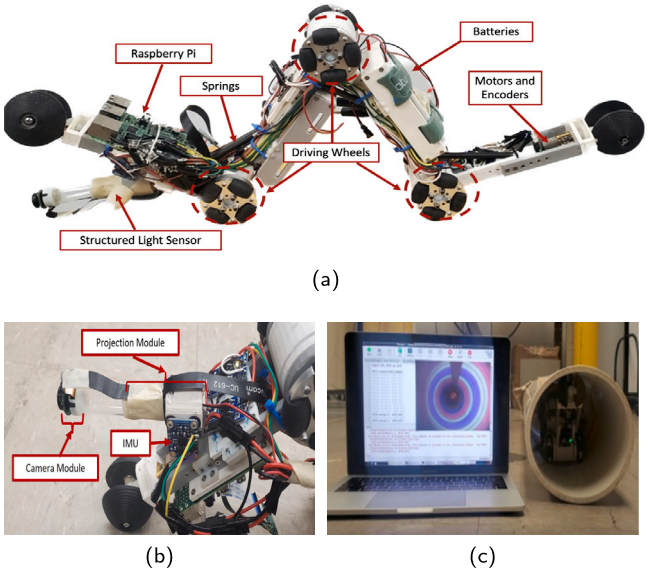

Fig. 8. (a) Robotic platform with integrated SL sensor; (b) Main component of SL sensor; (c) Real-time data collection and monitoring in 6-inch pipe.

3.4. Uncertainty source analysis

In pipeline inspection or field testing, a systematic investigation of the effects due to various uncertainties is essential for quantitative NDE and reliability analysis. Uncertainty quantification (UQ) is critical to quantitatively describing the quality and reflects the accuracy of detection, and ultimately the reliability of the complex systems. In this sensing system, any uncertainty or error in data acquisition, feature extraction, or subsequent analysis will inevitably affect the quality and reliability of the final reconstructed 3D data. Therefore, uncertainty quantification facilitates objective assessment of performance and provides a comprehensive analysis to show the relationship between the uncertainty involved and the final output, and thus provide a high reliability sensing system for pipeline inspection. Errors and uncertainties affecting the accuracy of this structured light 3D measurement system mainly come from three parts: the instruments, the processing method, and the environment.

1. From **Instrument Design**: A reliable and rigid mechanical design of the sensing system is important. Shadow effect of the sensor is one major uncertainty source, which deteriorates the reconstruction accuracy when dealing with abrupt height changes in the pipe surface. As mentioned in [13], this problem is caused by the current single camera and projector setup, which restricts the view angle. Low intensity of the light source and low resolution will cause poor imaging quality of the slide pattern, and thus may affect the measurement accuracy. Also, the accurate distance and direction measurements from the IMU and encoder are key factors in determining the alignment between the frames and accumulated error will lead to performance degradation of the localization. For the odometry input, according to the Eq. (25), possible error accumulation will arise from either the measurements of the wheel diameter and speed estimation.

(a) Wheel diameter: non-circular wheel shape because of the usage of omnidirectional wheels.

(b) Wheel slippage: wheel slippage while passing over obstacles or during turning, will cause perturbations in velocity measurements. The relation between the acquired wheel slip velocity V_s and the measured velocity (rotational speed) V_r can be described through a linear function with an unbiased Gaussian uncertainty U [23], which can be written as:

$$\mathbf{V_s} = (\mathbf{f}(\mathbf{V_r}) + \mathbf{U}) \tag{27}$$

while the uncertainty $U \sim \mathcal{N}(0, \sigma^2)$ is the unbiased Gaussian noise with zero mean and variance σ^2; $f(.)$ is first order polynomial fitting procedure with lease square estimate. Therefore, if slip is considered in future work, the wheel slip distance T_{ods}, defined in Eq. (25), can be obtained by velocity and duration Δt : $T_{ods} = V_s \cdot \Delta t$.

2. From **Method**: The calibration of the main components of the SL sensor, such as the camera, projector, and IMU, are essential to obtaining the relative parameters for further data analysis. Errors introduced by the imprecise parameter estimation of the sensing system will deteriorate the overall performance. Therefore, a reliable and efficient calibration method for each component is essential. For the following defect reconstruction and measurement, uncertainties from those processing models, such as the calculation error of the registration algorithm, also contribute to the uncertainty in the measurement result.
3. From **Environment**: The environment where tests and calibrations are performed can have an influence on uncertainty in measurement results. Vibration caused by the uneven pipe surface can introduce random errors into the measurements. Additionally, inadequate lighting conditions for measurements have a crucial impact on the imaging quality, which makes the slide patterns difficult to distinguish.

The measurement uncertainties will result in a decrease of the precision and accuracy of the reconstructed defect shape, which will be further investigated in Section 4.4.2

4. Evaluation of the IMU-assisted sensing system

4.1. Experimental setup

To demonstrate the IMU-assisted robotic sensing system, experiments were performed in a 6-inch diameter PVC pipe with two defects, The first scanned segment is from point A to B, and the second is from point B to C as shown in Fig. 9. Both defects have the same dimensions of 70 mm length, 35 mm width, and 7.5 mm depth. The sensor was first attached to a gantry and traverses the pipe. The inspection process starts at point A and moved towards point B. Upon reaching point B, the sensor is rotated about the z-axis and then the sensor is moved to point C. This inspection scenario simulates sensor rotation during an inspection with off-center sensor misalignment. Fig. 10 shows example structured light image frames, highlighting the sensor rotation between segments A to B, and B to C.

4.2. Comparison of 3D reconstruction methods

To evaluate the performance of the proposed cylindrical fitting-based registration algorithm, it is compared to two other methods. The first method is an ellipsoid fitting-based point cloud registration algorithm, which was previously developed by some of the authors of this work [13]. In this method, an ellipsoid is used to fit the cylindrical surface to handle pipes with oval shapes and errors from the sensor calibration and then estimate both the orientation of the sensor and its position inside the pipe for each acquired frame with followed

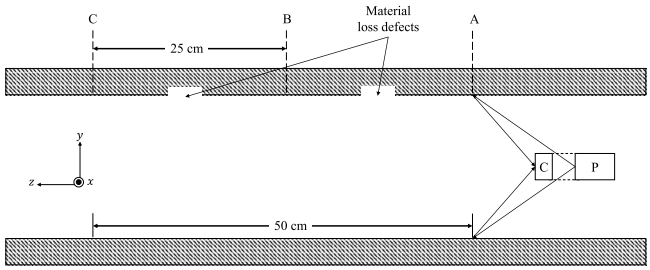

Fig. 9. Schematic of the test pipe.

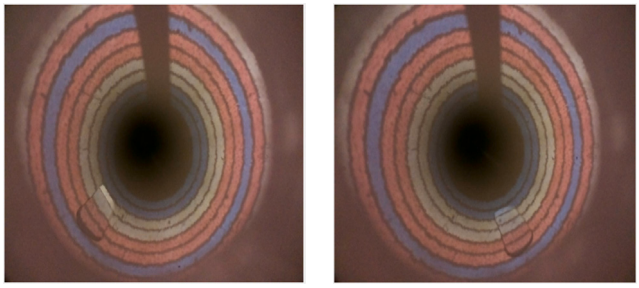

Fig. 10. Example image frame illustration (a) Point A to Point B; (b) Point B to Point C.

alignment correction. To register multiple frames, the corrected data is stacked by adding a constant displacement in the z-direction for each acquired frame, while keeping z-direction displacement constant by having a fixed scanning speed.

The second method is the Iterative Closest Point (ICP) algorithm, which is a classic registration method, commonly used to register 2D or 3D surfaces from different scans and to localize robots to achieve optimal path planning [24]. It is one of the approaches adopted in developing 3D models or building 3D world maps for SLAM [25–27]. The ICP algorithm helps find the transformation between a point cloud and a reference point cloud by minimizing the squared error between the corresponding entities. In this method, the initial frame is used as the reference to obtain the initial estimation of the transformation through a fitted plane. For the following frames, a point-to-plane distance metric minimization technique aligns each source point cloud with the combined estimation of rotation and translation. Similarly, the aligned frame will be stacked in the z-direction to reconstruct the pipe.

The comparison results are presented in Fig. 11. From the top view, it can be seen that the proposed registration algorithm retrieves a better pipe shape with a clearer and smoother boundary compared to the other two methods. Also, the marked defect area in the cylindrical-based method is more distinct and solid which is beneficial for defect isolation. Additionally, from the side view, the reconstructed 3D profile of the ICP-based method has a large misalignment after the sensor rotation, while the ellipsoid-based and the proposed cylindrical fitting-based method could fully reconstruct the 3D profile of the inspected pipe section. The main criterion of the registration algorithm is the ability to reconstruct the complete pipeline structure with less noise. Specifically, each data frame should be aligned vertically to build a straight and clear pipe surface. Therefore, a plane was applied to fit each reconstructed 3D point cloud pipe and extract the normal vector $\vec{\mathbf{n}_i}$ to obtain the directional information of each frame **i**. Since the pipe is a standard cylinder, projecting the 3D data frame onto the XY plane should theoretically result in a circle. The projected points are then fitted to a circle to obtain the estimated center location $\mathbf{O_{ci}}$ and radius $\mathbf{R_{ai}}$. The location of each frame can be reflected from the extracted center, which is highly related to the registration theory of each method.

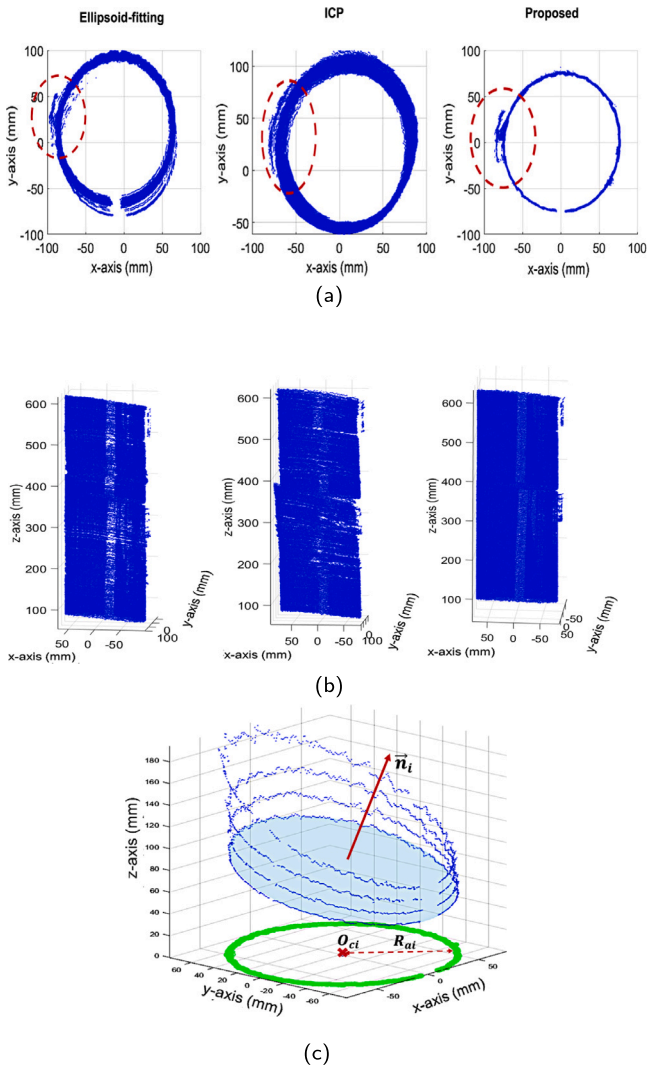

Fig. 11. Reconstruction performance comparison among Ellipsoid based (left), ICP-based (middle) and proposed Cylindrical (right) registration algorithm: (a) Top view: reconstructed defect area are marked by red-dotted circle; (b) Side view; (c) Illustration of evaluation parameters from one single frame for performance comparison.

For a well-registered model, the differences in estimated centers and in directional vectors should be small to ensure height alignment between frames. Also, in the horizontal direction, the estimated circle should approximate the actual pipe size, so the estimated radius is a good criterion for evaluating registration performance, which is interpreted as Closeness, and defined as:

$$Closeness = \frac{|\bar{R}_a - R_{GT}|}{R_{GT}} \cdot 100\%. \tag{28}$$

where $\bar{\mathbf{R}}_a$ is the average of the total estimated $\mathbf{R_{ai}}$ in each method. Therefore, the above shape-based parameters can be extracted from the reconstructed pipe to quantitatively evaluate the reconstruction of those three registration techniques, which are illustrated in Fig. 11(c). In this comparison work, total variances of the normal vectors, center locations, and radius closeness are obtained from each registration technique, which is shown in Table 1.

The results show that all three methods are able to correct the frame in a consistent direction with low variance in the estimated norm. However, the cylindrical-based algorithm has a much higher reliability for vertical frame alignments based on the low center variance. For the estimated radius, although all methods were able to obtain the pipe diameter with small differences, the largest error was 1.71% from the ellipsoid-based fitting method, while the proposed method had the highest accuracy. Overall, the proposed method has been shown to be robust and reliable in alignment correction. Theoretically, ICP registration has the advantage of very high accuracy, but the performances and registration efficiency are constrained by a good initial value, the small transformation between the two point clouds, and small occlusion [28,29]. In this case, especially during the rotation, there exists a large misalignment between two point clouds, where the defect location is changed and the baseline of the whole frame is shifted. In addition, traditional ICP registration relies purely on geometry, color, or meshes, and thus cannot perfectly restore the defect area, especially when the initial point cloud is not able to contain the full defect information. In the proposed algorithm, however, the defect is considered as the feature, which could allow the reconstruction of the pipe and defects with higher reliability and are robust to a baseline shift. Considering the quality of reconstructed pipe shapes and defects, the proposed cylindrical-based 3D registration algorithm outperforms the state-of-the-art methods compared in this work.

Table 1
Reconstruction quality evaluation for registration techniques.

	Normal variance (mm)	Center variance (mm)	Radius closeness
Ellipsoid	0.001	1.507	1.71%
ICP	0.002	9.112	1.55%
Cylindrical	**0.001**	**0.025**	**0.95%**

4.3. Effect of using IMU

All of the registration methods listed in Section 4.2 failed to correct the rotation of the sensing platform around the main axis of the pipe. Therefore, IMU data was acquired in real-time with the camera data and then used to correct the data alignments according to the procedure described in Section 3.2.2. To illustrate the sensitivity and efficacy of the IMU, two experiments were performed at different rotation angles (8 degrees and 25 degrees) from point B to point C.

The 3D reconstructed profile after incorporating the IMU data with the proposed cylindrical-based registration is shown in Fig. 12. From the top and side views, it can be noticed that after integrating the IMU information, the position of the second defect is corrected to a similar vertical orientation to the first defect in both cases. Specifically, in Fig. 12(b), the estimated angle between two defects in z-axis with IMU assistance is corrected from 8 degrees to 2.3 degrees, while the change in Fig. 12(d) is corrected from 25 degrees to 3.3 degrees. Even with a relatively small rotation angle (8 degrees), the IMU is sensitive enough to capture changes in rotation and was found to create precise orientation readings. Experimental results show that the proposed registration algorithm with the IMU data incorporated was sufficient to reconstruct the defect adequately, which provides a good basis for applying cylindrical-based 3D registration to facilitate more reliable data reconstruction.

4.4. Integration with robotic platform

For testing the robot-integrated sensing system, the robot navigated from point A to point B in the 6-inch pipe. The acquired instantaneous position from the wheel encoders was deployed to adjust the stacking distance between each reconstructed frame; therefore, the reconstructed map will be able to provide a more accurate defect point cloud. The reconstructed pipe is presented in Fig. 13. To better illustrate the effectiveness and robustness of the robotic integrated platform, the reconstructed defect size was estimated based on experimental data for comparison with the ground truth defect size.

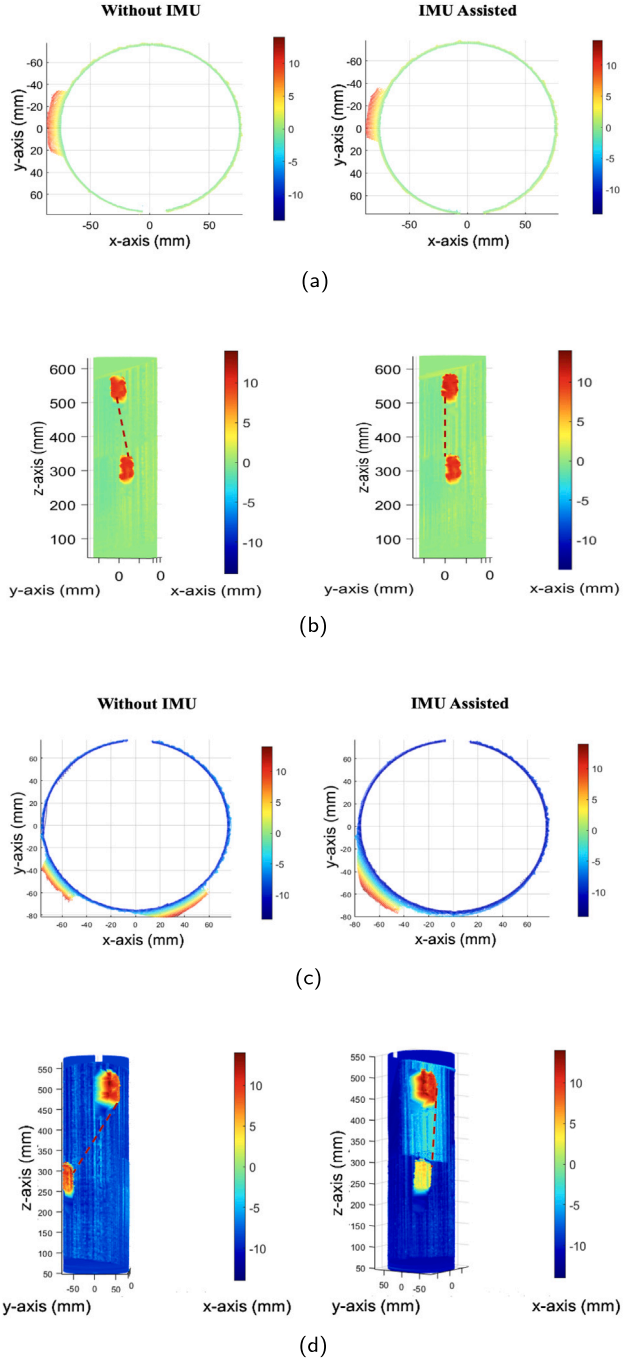

Fig. 12. Reconstruction performance without IMU (left) and with IMU (right). Rotation angle: 8 degree: (a) Top view; (b) Side view, Rotation angle: 25 degree; (c) Top view; (d) Side view.

4.4.1. Reconstruction performance in defect size estimation

The size estimation was converted to a segmentation problem, starting with flattening the reconstructed 3-D Point cloud to the cylindrical domain. The following defect length and width estimation procedure is realized through a proposed Intensity-based Threshold Searching algorithm, as illustrated in Fig. 14.

First, the intensity histogram is used to obtain **N** intensity clusters and then extract the mean of each cluster: $\mathbf{M_i} : \mathbf{M_1}, \mathbf{M_2}, \ldots, \mathbf{M_N}$; Next, based on each $\mathbf{M_i}$, the binarized cylindrical defect map $\mathbf{B_i}$ is generated for the following defect segmentation to obtain the estimated length $\mathbf{L_i}$ and width $\mathbf{W_i}$; Then by evaluating the distance between the estimated

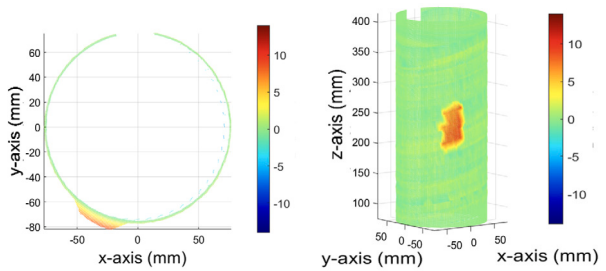

Fig. 13. Reconstruction performance with robotic integration: (a) Top view; (b) Side view.

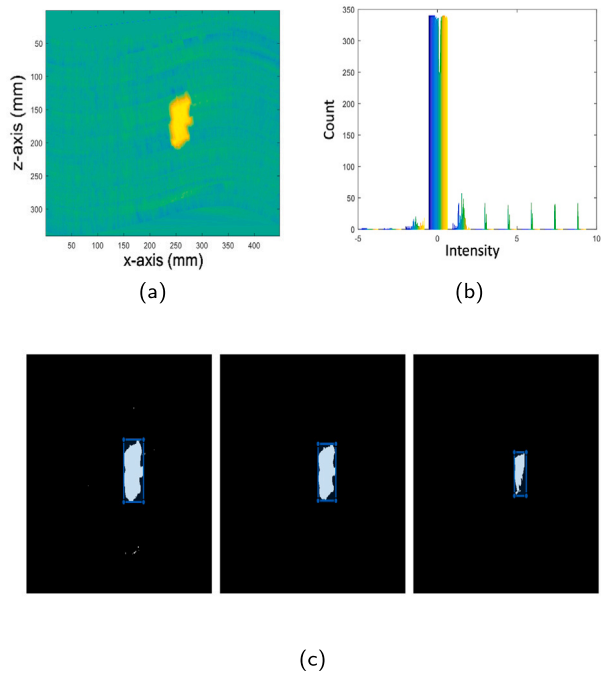

Fig. 14. Intensity-based Threshold Searching Procedure: (a) Cylindrical defect map; (b) Intensity histogram; (c) Binarized candidate examples with the segmented defect.

size and the true defect size L_{GT} and W_{GT}, an error estimation is deployed for selecting the best candidate, which is described as follows:

$$Err_i = 0.5 * \sqrt{(\frac{L_i - L_{GT}}{L_{GT}})^2 + (\frac{W_i - W_{GT}}{W_{GT}})^2}. \tag{29}$$

By selecting the minimal Err, the corresponding cluster $\mathbf{M}_{optimal}$ is obtained as the optimal threshold, and thus the optimal estimated defect length $\mathbf{L}^*$ and Width $\mathbf{W}^*$ are created.

Furthermore, the significance of determining defect depth lies in its critical role in assessing the impact of a defect on the structural integrity of a component or material. In this application, the process of reconstructing the defect depth begins with the extraction of a 3D point cloud representing the defect region, as illustrated in Fig. 15. The 3D defect map is initially converted to the $Y - Z$ axis, and then the defect information is isolated to obtain the average background information B. This background information is utilized to fill in the defect area, resulting in the final construction of a complete 3D plot that accurately represents the defect in relation to its reconstructed depth. Since the true defect surface has some inherent roughness, and from the full map, the variation in defect depth can be observed, which provides a good basis for understanding the inspected defect. As the industry focuses on

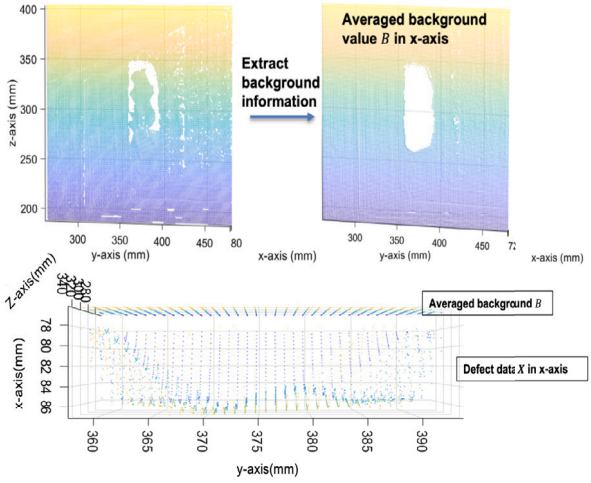

(a)

Fig. 15. Defect depth estimation procedure.

Table 2
Estimated defect size and *Error* in repetition tests.

	Test 1	Test 2	Test 3	Test 4	Test 5	Test 6
Length (mm)	67.2	72.3	67.7	71.3	76.6	66.1
Width (mm)	34.2	35.7	33.1	31.3	35.2	32.6
Err	2.3%	1.9%	3.2%	5.4%	4.7%	4.4%
Depth (mm)	5.7	8.6	9.4	4.7	5.6	4.8
Error	8.2%	5.1%	8.7%	12.9%	9.0%	12.4%

determining the maximum wall loss, only the largest estimated depth measurement is taken into consideration in this case.

To investigate the accuracy of the reconstructed measurements, the estimated length L_i, width W_i, and depth D_i are compared to the ground truth defect size L_{GT}, W_{GT}, and D_{GT}. This evaluation involves an error estimation equation that considers the differences in length, width, and depth simultaneously. The equation for evaluating the overall size estimation performance is as follows:

$$Error_i = \frac{\sqrt{(\frac{L_i - L_{GT}}{L_{GT}})^2 + (\frac{W_i - W_{GT}}{W_{GT}})^2 + (\frac{D_i - D_{GT}}{D_{GT}})^2}}{3} \tag{30}$$

Given the presence of uncertainties in the reconstruction results, the calculated values of *Err* and *Error* serve as reliable estimations for the length-width of the defect and the overall uncertainty in this sensing system based on 3D reconstruction. To better evaluate the reconstruction performance, six repeated scans ($i = 6$) with the robotic platform were conducted, where the results are presented in Table 2. The results indicate that there is variation observed in the reconstructed defect sizes, and the error in the overall size estimation can be as high as 12.9%. However, when considering the estimated *Err*, the differences between the estimated defect size and the ground truth defect are relatively small, staying within 6%. Therefore, the proposed registration and subsequent defect estimation algorithm employed in this IMU-assisted SL sensing system have been demonstrated to effectively uncover genuine defect information, particularly in accurately estimating defect length and width with a high level of precision. Furthermore, the applied robotic system has proven to enable an efficient and robust multiple data collection system via SLAM capabilities.

4.4.2. Measurement uncertainty analysis

The uncertainty of the entire system does not only come from the known uncertainty source; measurements and the following analysis procedures also contribute to the uncertainty. Therefore, it is difficult

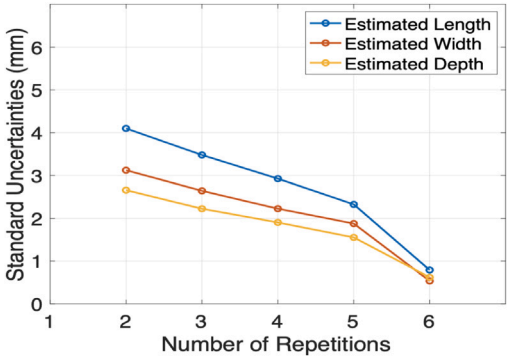

Fig. 16. Comparison results of expanded uncertainty with GUM.

to quantify the relationship between inputs and measured outputs directly. The Guide to the Expression of Uncertainty in Measurement (GUM), is the most commonly used method to analyze measurement uncertainty, which can reflect all propagated uncertainties relevant to the measurement and thus is instrumental in evaluating the quality of measurements. In the content of the GUM model, the measurement uncertainty is obtained from three aspects: repeatability, reproducibility, and maximum indication error of the instrument. Repeatability denotes changes in measurement data during repeated measurements under the same condition, whereas with reproducibility, measurement data changes are caused by changing measurement conditions [30]. Considering there are no other measurement methods, measurement instruments, or operators involved in this work, the GUM-based uncertainty analysis of repeatability is addressed only based on the six reconstruction results presented in Table 2.

In this process, the mean square is an approximation of the variance of the measured value under the same conditions. The standard deviation combination S of multiple measurement n is considered as standard measurement uncertainty. Further, according to GUM, an expanded uncertainty is applied to provide coverage with 95% confidence when $k = 1.96$, therefore the measurement uncertainty is expressed as:

$$\begin{aligned} U_{extend} &= k * U_{standard} = k * \frac{S}{\sqrt{N}} \\ &= k * \sqrt{\frac{1}{N(n-1)} \sum_{i=1}^{n} (y_i - \bar{y})^2} \end{aligned} \tag{31}$$

where the mean value of N repeat measurements is considered as the optimal representation; y_i is the ith measurement value; and $\bar{y}$ is the average value of repeated measurements [31]. To track the relationship between the number of repetitions and the uncertainty, K-combinations were applied for each repeated measurement to increase the reliability and variety of the tests. Specifically, the standard deviation is calculated from measurements with possible combinations of measurements $\binom{\mathbf{n}}{\mathbf{m}}$ depending on **m** and then the average standard deviation in those from **n** choose **m** combinations are taken to obtain the standard uncertainty for repetitions from 1 to **n** [32]. The standard uncertainties in the estimated defect length and width are computed separately, shown in Fig. 16.

The result shows that measurement uncertainties are correlated with the number of repetitions, where the uncertainties decreased as the number of repetitions increased, which proves the importance of repeat measurements for uncertainty reduction. Overall, the uncertainty of the length estimation is much smaller than that of the width, and since the frame distance is one of the main factors in determining the length, the accuracy and robustness of the odometer and IMU sensors in position correction are demonstrated. According to Eq. (31), the measurement uncertainty interval can be determined by considering

Table 3
Measurement uncertainty evaluation.

Measurement uncertainty	Standard	Expanded, k = 1.96
Length (mm)	0.79	1.55
Width (mm)	0.54	1.05
Depth (mm)	0.62	1.22

Table 4
Percentage wall loss evaluation.

Wall loss (%)	Depth (mm)	Averaged estimated depth (mm)	Quality (%)
75%	5.63	5.2	88.5
50%	3.75	2.7	72.0
25%	1.88	1.2	63.5

the estimated length and width of all six measurements, which are presented in Table 3.

As can be seen from measurement uncertainty, by taking a 95% coverage probability, the obtained expanded uncertainty is considered as the best estimate of the correction with the measurement error. The length is estimated to be 70.5 ± 1.55 mm, the width is 33.7 ± 1.05 mm, and the depth is 6.1 ± 1.22 mm. Although the number of repetitions is limited, the initial error estimates and analysis of measurement uncertainty provide a strong foundation for showcasing the potential of uncertainty estimates provided by the GUM. Furthermore, given the capability of the integrated robotics platform to support multiple SLAM-based data collections, a more robust and holistic uncertainty estimation model can be constructed by performing more experiments.

4.4.3. Performance evaluation for varied defect depth and shape

In industrial applications, the assessment of Percentage Wall loss (%WL) through NDE inspection is of utmost importance for ensuring structural integrity and overall safety. Additionally, the presence of irregularly shaped defects adds further complexity to the inspection process. Therefore, we further explore the depth estimation and irregular shape estimation capabilities of the proposed SL sensor in this section.

In our previous investigation, we focused on analyzing the reconstruction performance of the defect with 100% WL. Now, we have extended our study by adjusting the depth of the defect to different levels, specifically 75%, 50%, and 25% WL. This adjustment reflects a reduction in the magnitude of wall loss. To quantitatively assess the quality of depth reconstruction, three measurements are obtained for each scenario. The depth estimation quality is evaluated using the following formula:

$$D_{Quality} = 1 - D_{err_i} = 1 - \frac{1}{N}\sum_{i=1}^{N}\left(\frac{|D_i - D_{GT}|}{D_{GT}}\right) \tag{32}$$

where |.| denotes the absolute value. The estimation quality is determined by the average percentage difference between the estimated depth and the actual depth over N times measurements. The results of these averaged depth estimations are presented in Table 4. The results indicate that the proposed method successfully retrieves defect depth information for varying extents of wall loss. The accuracy of the depth estimation improves as the defect depth increases, reaching up to 88.5% for the 75% WL defect. The shallowest defect with a depth of 1.88 mm, although may have a higher estimated error compared to the deeper defects, is still detectable.

Furthermore, reconstructed cylinders for each of the changed depths are shown in Fig. 17. The corresponding results effectively highlight the variations in the shape of the reconstruction as the defect depth diminishes. Overall, all kinds of defect shapes are able to be depicted, especially for the 75% WL and 50% WL case, which provides clear visibility and characterization of the defect. However, for very shallow depths of 25% WL, although the defect area can still be highlighted,

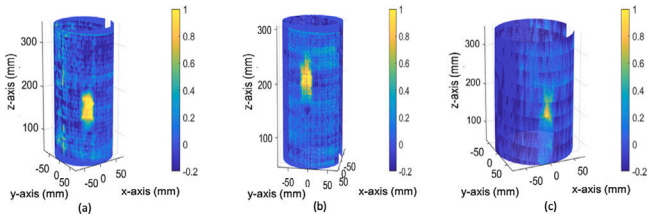

Fig. 17. Reconstruction performance comparison among different %WL: (a) 75%WL; (b) 50%WL; (c) 25%WL.

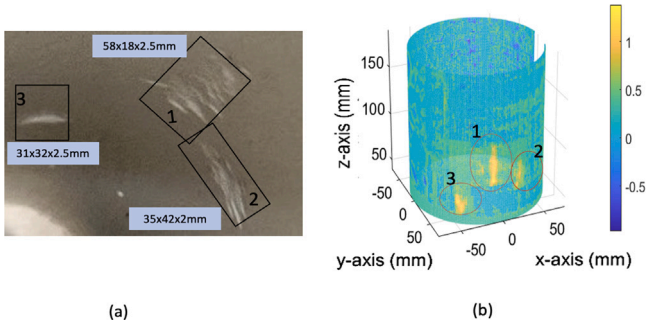

Fig. 18. (a) Scratch-like defects; (b) Reconstruction performance of scratch-like defects.

the differentiation and completion of the defect edges become more difficult. Therefore, as the defect depth decreases, the defect edges may appear less distinct or fragmented, potentially resulting in an incomplete representation of the defect's shape and boundaries. The main reason for the correlation between defect depth and the detection performance of the proposed SL sensor is attributed to its detection principle. In detail, deeper defects will cause more significant distortions in the projected color pattern, resulting in clearer and more distinguishable outliers. Therefore, the subsequent registration process can effectively identify and isolate these outliers, facilitating accurate defect detection and localization.

Moreover, unlike uniform or regular defects, scratch-like defects can have complex geometries and inconsistent depths. Detecting and characterizing scratch-like defects allows us to gain insights into the system's performance in detecting and characterizing defects with diverse geometric characteristics. In this study, three scratch-like defects with various shapes and depths in the pipe are investigated. As the varying shape and depth are difficult to track, the maximum length, width, and depth of each defect are measured, which serves as a reference. The scratch-like defects and estimated size are shown in Fig. 18(a).

From the reconstructed cylinder depicted in Fig. 18(b), it can be seen that although the complete shape of the scratch-like defects cannot be clearly reconstructed due to their shallow depth and irregular shapes, the system is able to detect and locate these shallow defects. This demonstrates the capability of the proposed system to identify and characterize minor surface irregularities, even when the depth and shape information is limited. Besides, while defect 2 has a larger maximum size compared to defect 3, its lower %WL results in reduced shape information, evident in the lower intensity level and less distinct defect edges. This emphasizes the importance of defect depth in the reconstruction process, where accurate depth estimation significantly contributes to the overall effectiveness and reliability of the system in capturing and characterizing defects of varying shapes. Overall, the sensitivity of the proposed system in identifying minor irregularities or deformations on the inner pipe surface has been highlighted, demonstrating its capability in detecting even subtle defects.

5. Conclusion

This paper proposes a comprehensive and practical IMU-assisted robotic SL sensing system with enhanced registration and defect estimation solutions for pipeline detection. The framework relies on a RANSAC-assisted cylindrical fitting registration algorithm and inertial and odometry measurements for obtaining the global and local positioning, which enables accurate 3D profiling. Instead of a direct matching of the point clouds, the proposed registration algorithm exploits the geometry of the pipe and certain sensor characteristics to enable accurate registration even in the presence of defects. The input from IMU is critical for accurate data reconstruction in the presence of rotation and the absence of features by accurately correcting the rotation in the experiment. The wheel encoder provides a precise robot location, which is beneficial for concurrent 3D data registration and defect measurement. Furthermore, the uncertainty sources in this SL-based sensing system are described in detail, providing a guide for future uncertainty analysis. The proposed registration algorithm is first validated with both simulations and experimental data. Based on the selected shape-based parameters, the proposed registration method is proven to be more efficient and reliable compared to other states of art methods like ICP. The results show that the proposed framework is able to provide a robust and reliable 3D defect reconstruction solution in terms of varying defect shape and depth. The robot-enabled SL sensing system is able to provide reliable and robust repeated measurements, which provide a basis for a more accurate measurement uncertainty estimation with the GUM-based uncertainty model. Therefore, the proposed integration work shows great potential for high reliability and efficiency in visual-based pipeline inspection.

CRediT authorship contribution statement

Mohand Alzuhiri: Conceptualization, Methodology, Writing – original draft. **Zi Li:** Conceptualization, Methodology, Writing – original draft. **Adithya Rao:** Data curation, Experiment implementation. **Jiaoyang Li:** Writing – review & editing. **Preston Fairchild:** Experiment implementation. **Xiaobo Tan:** Writing – review & editing. **Yiming Deng:** Supervision.

Declaration of competing interest

The authors declare that they have no known competing financial interests or personal relationships that could have appeared to influence the work reported in this paper.

Data availability

The data that has been used is confidential.

References

[1] Vetter CP, Kuebel LA, Natarajan D, Mentzer RA. Review of failure trends in the US natural gas pipeline industry: An in-depth analysis of transmission and distribution system incidents. J Loss Prev Process Ind 2019;60:317–33.

[2] Mora-Rodríguez J, Delgado-Galván X, Ramos HM, López-Jiménez PA. An overview of leaks and intrusion for different pipe materials and failures. Urban Water J. 2014;11(1):1–10.

[3] Maupin J, Mamoun M, et al. Plastic Pipe Failure, Risk, and Threat Analysis. Technical Report, Gas Technology Institute; 2009.

[4] Farshad M. Plastic Pipe Systems: Failure Investigation and Diagnosis. Elsevier; 2011.

[5] Zhu J, Collins RP, Boxall JB, Mills RS, Dwyer-Joyce R. Non-destructive in-situ condition assessment of plastic pipe using ultrasound. Procedia Eng. 2015;119:148–57.

[6] Wang Q, Zhou H, Xie J, Xu X. Nonlinear ultrasonic evaluation of high-density polyethylene natural gas pipe thermal butt fusion joint aging behavior. Int J Press Vessels Pip 2021;189:104272.

[7] Carrigan TD, Forrest BE, Andem HN, Gui K, Johnson L, Hibbert JE, Lennox B, Sloan R. Nondestructive testing of nonmetallic pipelines using microwave reflectometry on an in-line inspection robot. IEEE Trans Instrum Meas 2018;68(2):586–94.

[8] Haryono A, Abou-Khousa MA, et al. Microwave non-destructive evaluation of glass reinforced epoxy and high density polyethylene pipes. J Nondestruct Eval 2020;39(1):1–9.

[9] Kafieh R, Lotfi T, Amirfattahi R. Automatic detection of defects on polyethylene pipe welding using thermal infrared imaging. Infrared Phys Technol 2011;54(4):317–25.

[10] Doaei M, Tavallali MS. Intelligent screening of electrofusion-polyethylene joints based on a thermal NDT method. Infrared Phys Technol 2018;90:1–7.

[11] Li C, Lan H-Q, Sun Y-N, Wang J-Q. Detection algorithm of defects on polyethylene gas pipe using image recognition. Int J Press Vessels Pip 2021;191:104381.

[12] Karkoub M, Bouhali O, Sheharyar A. Gas pipeline inspection using autonomous robots with omni-directional cameras. IEEE Sens J 2020;21(14):15544–53.

[13] Alzuhiri M, Farrag K, Lever E, Deng Y. An electronically stabilized multi-color multi-ring structured light sensor for gas pipelines internal surface inspection. IEEE Sens J 2021.

[14] Chuang T-Y, Sung C-C. Learning and SLAM based decision support platform for sewer inspection. Remote Sens 2020;12(6):968.

[15] Kumar S. Development of SLAM algorithm for a Pipe Inspection Serpentine Robot 2019.

[16] Krys D, Najjaran H. Development of visual simultaneous localization and mapping (VSLAM) for a pipe inspection robot. In: 2007 International symposium on computational intelligence in robotics and automation. IEEE; 2007, p. 344–9.

[17] Zhang R, Evans M, Worley R, Anderson S, Mihaylova L. Improving slam in pipe networks by leveraging cylindrical regularity. In: Annual conference towards autonomous robotic systems. Springer; 2021, p. 56–65.

[18] Murtra AC, Tur JMM. IMU and cable encoder data fusion for in-pipe mobile robot localization. In: 2013 IEEE Conference on technologies for practical robot applications. IEEE; 2013, p. 1–6.

[19] Tang C-K. Tensor voting in computer vision, visualization, and higher dimensional inferences. University of Southern California; 2000.

[20] Geng J. Structured-light 3D surface imaging: a tutorial. Adv Opt Photon 2011;3(2):128–60.

[21] Shah M, Eastman RD, Hong T. An overview of robot-sensor calibration methods for evaluation of perception systems. In: Proceedings of the workshop on performance metrics for intelligent systems. 2012, p. 15–20.

[22] Tsai RY, Lenz RK, et al. A new technique for fully autonomous and efficient 3 D robotics hand/eye calibration. IEEE Trans Robot Autom 1989;5(3):345–58.

[23] Sidharthan RK, Kannan R, Srinivasan S, Balas VE. Stochastic wheel-slip compensation based robot localization and mapping. Adv Electr Comput Eng 2016;16(2):25–32.

[24] Besl PJ, McKay ND. Method for registration of 3-D shapes. In: Sensor fusion IV: control paradigms and data structures, vol. 1611. Spie; 1992, p. 586–606.

[25] Tiar R, Lakrouf M, Azouaoui O. FAST ICP-SLAM for a Bi-steerable mobile robot in large environments. In: 2015 IEEE International workshop of electronics, control, measurement, signals and their application to mechatronics. IEEE; 2015, p. 1–6.

[26] Costa WF, Matsuura JP, Santana FS, Saraiva AM. Evaluation of an ICP based algorithm for simultaneous localization and mapping using a 3D simulated P3DX robot. In: 2010 Latin American robotics symposium and intelligent robotics meeting. IEEE; 2010, p. 103–8.

[27] Wang Y, Xiong R, Li Q. EM-based point to plane ICP for 3D simultaneous localization and mapping. Int J Rob Autom 2013;28:234–44.

[28] Wang J-w, Wang M. 3D reconstruction of shoe-last based on binocular stereo vision. Comput Technol Dev 2009;19:224–30.

[29] Cheng L, Chen S, Liu X, Xu H, Wu Y, Li M, Chen Y. Registration of laser scanning point clouds: A review. Sensors 2018;18(5):1641.

[30] Muscat S, Parks S, Kemp E, Keating D. Repeatability and reproducibility of macular thickness measurements with the Humphrey OCT system. Invest Ophthalmol Vis Sci 2002;43(2):490–5.

[31] Li S, Wang Z, Guan J, Wang J. Uncertainty evaluation in surface structured light measurement. In: 2021 IEEE 15th International conference on electronic measurement & instruments. IEEE; 2021, p. 395–400.

[32] Li Z, Shenoy BB, Udpa L, Udpa S, Deng Y. Magnetic barkhausen noise technique for early-stage fatigue prediction in martensitic stainless-steel samples. J Nondestruct Evaluat Diagn Prognostics Eng Syst 2021;4(4).

Update

NDT and E International

Volume 144, Issue , June 2024, Page

DOI: https://doi.org/10.1016/j.ndteint.2024.103081

NDT&E International 144 (2024) 103081

Contents lists available at ScienceDirect

NDT and E International

journal homepage: www.elsevier.com/locate/ndteint

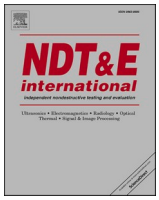

Corrigendum

Corrigendum to "IMU-assisted robotic structured light sensing with featureless registration under uncertainties for pipeline inspection" [NDT E Int 139 (2023) 102936]

Mohand Alzuhiri, Zi Li *, Adithya Rao, Jiaoyang Li, Preston Fairchild, Xiaobo Tan, Yiming Deng

Department of Electrical and Computer Engineering at Michigan State University, East Lansing, MI, 48824, USA

The authors regret to inform that the project number is wrongly added in the published version. The correct one should be: 'This work was supported in part by the United States, Department of Transportation, Pipeline and Hazardous Materials Safety Administration (693JK32050002CAAP)'.>

The authors would like to apologise for any inconvenience caused.

DOI of original article: https://doi.org/10.1016/j.ndteint.2023.102936.

* Corresponding author.
E-mail address: lizi4@msu.edu (Z. Li).

https://doi.org/10.1016/j.ndteint.2024.103081

Available online 25 February 2024